Variable Amplitude Pulsating Signal Injection Method With Low DC-Bus Voltage Occupancy for Sensorless Control of IPMSM

Junli Huang, *Graduate Student Member, IEEE*, Shanming Wang, *Senior Member, IEEE*, and Wenmao Liu, *Member, IEEE*

***Abstract*—Sensorless control based on signal injection is inherently limited to low-speed operation due to the injection voltage occupying the dc-bus voltage. This article proposes a variable amplitude pulsating signal injection method with low dc-bus voltage occupancy for sensorless control of interior permanent-magnet synchronous motors. The varying injection amplitude is dynamically determined by both the fundamental three-phase voltage and the dc-bus voltage. A demodulation system is designed to extract the amplitudes of the response current. The sinusoidal-varying instantaneous susceptance signal, which is the amplitude ratio of the response current to the injection voltage, is introduced to obtain the rotor position. The effectiveness of the proposed method is validated through simulations and experiments. The proposed method significantly reduces the voltage occupancy of the injection signal to merely 5% of the dc-bus voltage, which extends the operational speed range of signal injection methods.**

***Index Terms*—Low dc-bus voltage occupancy, sensorless control, signal injection, variable voltage injection.**

I. Introduction

PERMANENT-MAGNET synchronous motors (PMSMs) are widely used in industrial applications. In order to reduce costs or enhance system reliability, sensorless control methods have been extensively investigated.

Sensorless control methods can be categorized into two types based on their principles [1], [2], [3]. The first type is the back electromotive force (back EMF) or flux methods. These methods estimate motor position from the back EMF of the motor and are suitable in high-speed scenarios, while they become ineffective in low-speed conditions as the EMF diminishes to an undetectable level. The second type is the saliency-based methods. This approach, also known as the signal injection method, involves injecting signals to extract the reluctance differences at various rotor positions, thereby determining the rotor position. Signal injection methods exhibit a lower dependence on motor parameters compared to model-based approaches. They demonstrate superior system robustness under parameter mismatches and variations due to saturation. Moreover, signal injection methods can achieve high-performance position estimation at low and zero speeds, a capability that model-based methods struggle to match. This article focuses on the signal injection method.

Signal injection methods are categorized by the reference frame for injection into two primary types [1], [2], [3]: synchronous rotating reference frame (SRRF) [4], [5], [6], [7], [8], [9], [10], [11], [12] and stationary reference frame (SRF) [13], [14], [15], [16], [17], [18], [19], [20], [21], [22]. The SRRF type is simpler due to no complex filtering, while the SRF type offers better robustness as the injection signal is independent of position estimation [1].

The SRRF injection method suffers from stability issues, as its stability relies on the accuracy of rotor position estimation results. It only works when the estimated speed matches the actual speed, enabling convergence. Once deviating from equilibrium, SRRF fails to reconverge, resulting in poor robustness [16], [17]. To overcome this problem, the SRF methods gain attention because of their ability to reconverge even if the position estimation system deviates from the equilibrium point.

Signal injection methods are also categorized by their waveforms into two primary types [1], [2], [3]: sinusoidal and square-wave signal injection. The sinusoidal type uses low injection frequency to reduce the injection voltage, but introduces torque ripples [7], [9], [10], [12], [13], [15], [17], [18], [19], [20], [21], [22], [23], [24]. The square-wave type has a higher injection frequency, which can achieve better dynamic performance, leading to broader application scenarios [4], [5], [6], [8], [11], [14], [16], [25].

For signal injection methods, a proportion of the dc-bus voltage is required to obtain rotor information. At high motor speeds, when back EMF is high, signal injection methods are often limited by the available voltage and thus are not used. Consequently, signal injection methods are generally applied only in low-speed scenarios. Researches suggest that a minimum threshold for injection voltage amplitude is required to ensure system stability, which is proportional to the negative sequence inductance of the motor and the frequency of the injection signal [20].

Received 27 June 2025; revised 13 October 2025; accepted 22 November 2025. Date of publication 26 November 2025; date of current version 25 February 2026. This work was supported by Smart Grid-National Science and Technology Major Project 2025ZD0805800. Recommended for publication by Associate Editor Y. A.-R. I. Mohamed. *(Corresponding author: Wenmao Liu.)*

The authors are with the State Key Laboratory of Power System Operation and Control, Department of Electrical Engineering, Tsinghua University, Beijing 100084, China (e-mail: jl-huang21@mails.tsinghua.edu.cn; wangsm96@mails.tsinghua.edu.cn; wenmaoliu@tsinghua.edu.cn).

Color versions of one or more figures in this article are available at https://doi.org/10.1109/TPEL.2025.3637284.

Digital Object Identifier 10.1109/TPEL.2025.3637284

TABLE I
DC-BUS VOLTAGE OCCUPANCY RATIO IN RECENT SIGNAL INJECTION METHODS

Source	Carrier waveform in modulation	Reference frame	DC-bus voltage occupancy ratio
[14]	square-wave	SRF	22.7%
[18]	square-wave	SRF	25.8%
[11]	square-wave	SRF	32%
[6]	square-wave	SRRF	37%
[4]	square-wave	SRRF	37%
[16]	square-wave	SRF	37%
[8]	square-wave	SRRF	40%
[21]	sinusoidal	SRRF	7.44%
[9]	sinusoidal	SRRF	21.1%
[20]	sinusoidal	SRRF	25.6%
[17]	sinusoidal	SRF	25.8%
[19]	sinusoidal	SRF	34.3%
[12]	sinusoidal	SRRF	37%
[13]	sinusoidal	SRF	71%

Conventional signal injection methods failed to operate at rated speed due to the voltage limitation. To evaluate the high-speed operation potential, this article introduces a key parameter for assessing the voltage utilization of signal injection methods: the dc-bus voltage occupancy ratio. The dc-bus voltage occupancy ratio refers to the proportion of the dc-bus voltage occupied by the injection signal, which is unavailable for generating the fundamental voltage of the motor, thereby limiting the maximum achievable speed. Table I summarizes the dc-bus voltage occupancy ratio of signal injection methods reported in the literature. A high dc-bus voltage occupancy ratio is required in the square-wave injection methods, which is above 22.7% as listed in Table I, as high injection frequencies are used to achieve better dynamic performance. In addition, the occupancy ratio of the sinusoidal injection methods is equally high as the square-wave type, except in [21]. The reason for the low occupancy ratio in [21] lies in the low injection frequency of only 500 Hz. However, such a low injection frequency induces significant torque pulsations and leads to instability in the control system.

In this article, a variable amplitude pulsating signal injection method in the SRF is proposed to achieve low dc-bus voltage occupancy for sensorless control. The proposed method selectively injects voltage in the zero-crossing regions of the fundamental voltage, while avoiding injecting voltage on the peaks, thereby achieving a low dc-bus voltage occupancy. To obtain the rotor position under varying injection voltage, this article introduces an instantaneous susceptance signal and a demodulation system for extracting the amplitude of response currents. The proposed method can reduce the voltage occupancy ratio to 5%, thus extending the speed range of signal injection sensorless control.

The rest of this article is organized as follows. In Section II, the principle and the disadvantages of the conventional signal injection method are introduced. In Section III, the principle and the implementation of the proposed signal injection method are presented. In Sections IV and V, the proposed method is validated by both simulations and experiments. Finally, Section VI concludes this article.

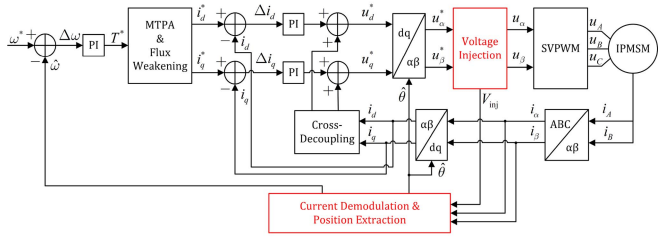

Fig. 1. Schematic diagram of the control system with SRF injection method.

II. CONVENTIONAL PULSATING SIGNAL INJECTION SENSORLESS METHOD

The structure of an SRF signal injection sensorless field-oriented control (FOC) system is illustrated in Fig. 1, where the two red blocks represent the voltage signal injection and the demodulation process for extracting rotor position from the response currents, respectively.

A. High-Frequency Signal Model of Interior PMSM (IPMSM)

Neglecting the harmonics and saturation effects of IPMSMs, the voltage equations in the dq reference frame can be written as

$$\begin{cases} v_d = R_s i_d + L_d \frac{\mathrm{d}i_d}{\mathrm{d}t} - \omega L_q i_q \\ v_q = R_s i_q + L_q \frac{\mathrm{d}i_q}{\mathrm{d}t} + \omega L_d i_d + \omega \psi \end{cases} \tag{1}$$

where v_d and v_q are the voltages on the d- and q-axes, i_d and i_q are the currents, and L_d and L_q are the inductance. R_s is the stator resistance. ψ is the flux linkage of the magnet. ω is the electrical angular speed of the rotor.

When the frequency of the injection signal is significantly higher than the speed of the motor in angular frequency, the stator resistance and the back EMF can be neglected, then the high-frequency voltage equations can be written as

$$\begin{cases} v_{d\mathrm{h}} = L_d \frac{\mathrm{d}i_{d\mathrm{h}}}{\mathrm{d}t} \\ v_{q\mathrm{h}} = L_q \frac{\mathrm{d}i_{q\mathrm{h}}}{\mathrm{d}t} \end{cases} \tag{2}$$

where $v_{d\mathrm{h}}$ and $v_{q\mathrm{h}}$ are the high-frequency components of the voltages on the d- and q-axes, and $i_{d\mathrm{h}}$ and $i_{q\mathrm{h}}$ are those of the currents.

The high-frequency model in the α–β reference frame is expressed as follows, which is used in the signal injection method in SRF [9], [13], [16]

$$\begin{cases} \frac{\mathrm{d}i_{\alpha\mathrm{h}}}{\mathrm{d}t} = \left(\frac{1}{L_\mathrm{S}} + \frac{1}{L_\mathrm{D}}\cos 2\theta\right) v_{\alpha\mathrm{h}} + \left(\frac{1}{L_\mathrm{D}}\sin 2\theta\right) v_{\beta\mathrm{h}} \\ \frac{\mathrm{d}i_{\beta\mathrm{h}}}{\mathrm{d}t} = \left(\frac{1}{L_\mathrm{D}}\sin 2\theta\right) v_{\alpha\mathrm{h}} + \left(\frac{1}{L_\mathrm{S}} - \frac{1}{L_\mathrm{D}}\cos 2\theta\right) v_{\beta\mathrm{h}} \end{cases} \tag{3}$$

where θ is the rotor position. $v_{\alpha\mathrm{h}}$ and $v_{\beta\mathrm{h}}$ represent the high-frequency components of the voltages on α- and β-axes, while

$i_{\alpha\mathrm{h}}$ and $i_{\beta\mathrm{h}}$ denote that of the currents. The symmetric inductance L_S and differential inductance L_D are defined as

$$L_\mathrm{S} = \frac{2L_dL_q}{L_q + L_d}, \quad L_\mathrm{D} = \frac{2L_dL_q}{L_q - L_d}.$$

B. Pulsating Signal Injection Method in SRF

In SRF, injecting a signal into the α-axis produces response currents in both the α- and β-axes, which contain rotor position information.

When injecting a high-frequency square-wave voltage into the α-axis at half the sampling frequency, the voltages are given by

$$\begin{cases} v_{\alpha\mathrm{h}} = \begin{cases} V_\mathrm{inj} & t \bmod 2T_\mathrm{s} \in [0, T_\mathrm{s}) \\ -V_\mathrm{inj} & t \bmod 2T_\mathrm{s} \in [T_\mathrm{s}, 2T_\mathrm{s}) \end{cases} = V_\mathrm{inj} \cdot f_\mathrm{h}(t) \\ v_{\beta\mathrm{h}} = 0 \end{cases} \tag{4}$$

where V_inj is the amplitude of injection voltage. T_s is the sampling period of the discrete-time control system. f_h is the square-wave carrier function.

According to the high-frequency model in the α–β reference frame (3), the increments of currents are as follows:

$$\begin{cases} \Delta i_\alpha \approx \Delta i_{\alpha\mathrm{h}} = \left(\frac{1}{L_\mathrm{S}} + \frac{1}{L_\mathrm{D}}\cos 2\theta\right) T_\mathrm{s} V_\mathrm{inj} \cdot f_\mathrm{h}(t) \\ \Delta i_\beta \approx \Delta i_{\beta\mathrm{h}} = \left(\frac{1}{L_\mathrm{D}}\sin 2\theta\right) T_\mathrm{s} V_\mathrm{inj} \cdot f_\mathrm{h}(t) \end{cases} \tag{5}$$

where Δi_α and Δi_β are the increments of α- and β-axes current between two adjacent samplings, and $\Delta i_{\alpha\mathrm{h}}$ and $\Delta i_{\beta\mathrm{h}}$ are the increments of the high-frequency components.

Demodulating the high-frequency component of the α-axis current by multiplying the increment of current with the carrier function, the resulting signal is obtained as

$$i_{\alpha\mathrm{res}} = \Delta i_\alpha \cdot f_\mathrm{h}(t) = V_\mathrm{inj} T_\mathrm{s} \frac{1}{L_\mathrm{S}} + I_\mathrm{inj} \cos 2\theta \tag{6}$$

where the amplitude of the varying part is

$$I_\mathrm{inj} = V_\mathrm{inj} T_\mathrm{s} \frac{1}{L_\mathrm{D}}. \tag{7}$$

Applying a high-pass filter to remove the dc component, the resulting signal is obtained as

$$\mathrm{HPF}[i_{\alpha\mathrm{res}}] = I_\mathrm{inj} \cos 2\theta. \tag{8}$$

Similarly, demodulating the high-frequency component of the β-axis current yields the following signal:

$$i_{\beta\mathrm{res}} = \Delta i_\beta \cdot f_\mathrm{h}(t) = I_\mathrm{inj} \sin 2\theta. \tag{9}$$

Rotor position information, contained in the orthogonal sinusoidal signals (8) and (9), can be extracted through an orthogonal phase-locked loop.

C. DC-Bus Voltage Occupancy Issues

Conventional signal injection methods employ a fixed-amplitude high-frequency injection voltage, which directly occupies the dc-bus voltage, and consequently, limits the achievable fundamental voltage amplitude.

Fig. 2 shows a schematic of the conventional SRF pulsating signal injection method. The amplitude of the injection voltage is constant [see Fig. 2(a)], while the resulting response current varies in amplitude according to the variation of inductance, manifesting as an amplitude-modulated high-frequency signal [see Fig. 2(b)]. The amplitude of response current [see Fig. 2(c)] is extracted by demodulation, then used to determine the rotor position.

Fig. 2(e) shows the waveform of the phase output voltage, which is obtained as the sum of the fundamental voltage [see Fig. 2(d)] and the injection voltage [see Fig. 2(a)]. The amplitude of the fundamental voltage is limited as the sum must not exceed the constant dc-bus voltage, shown as the dashed line in both Fig. 2(d) and (e). The injection signal restricts the amplitude of the fundamental voltage, particularly when approaching its peak, as shown in the blue-boxed region.

While this analysis specifically addresses signal injection methods in SRF, the tradeoff between the fundamental voltage and the injection voltage is inherently embedded in conventional signal injection methods, including the SRRF method.

III. Proposed Variable Amplitude Pulsating Signal Injection Sensorless Control

A. Principle of the Proposed Signal Injection Method

As mentioned in Section II-C, the injection voltage restricts the amplitude of fundamental voltage when approaching its peak, as shown in the blue-boxed region in Fig. 2. After carefully inspecting the waveform, in the zero-crossing regions of the fundamental voltage, the injection signal does not impose such limitations, as the green-boxed region shown in Fig. 2. As an improvement, the method with an injection voltage applied only in the zero-crossing regions is proposed to remove the limitation on the amplitude of the fundamental voltage.

Fig. 3 presents the proposed variable amplitude injection method, compared to Fig. 2. To reduce dc-bus voltage occupancy, the amplitude of injection voltage [see Fig. 3(e)] is adaptively adjusted based on the fundamental voltage waveform [see Fig. 3(f)]. This process transforms the injection voltage into an amplitude-modulated high-frequency signal [see Fig. 3(a)]. The amplitude of the resulting high-frequency response current [see Fig. 3(b)] further varies with the inductance, creating a *doubly amplitude-modulated* current signal [see Fig. 3(b) and (c)].

The *instantaneous susceptance* signal [see Fig. 3(d)], defined as the amplitude ratio of the response current to the injection voltage, is introduced to eliminate the influence of the varying amplitude of injection voltage, and to yield a sinusoidal signal directly correlated with the rotor position.

The key advantage of the proposed method lies in its ability to enable a higher amplitude of output voltage after signal injection with the same dc-bus voltage, as demonstrated by comparing Figs. 2(e) and 3(g). This characteristic is achieved by increasing the amplitude of the injection signal in zero-crossing regions of the fundamental voltage while reducing it near the peaks.

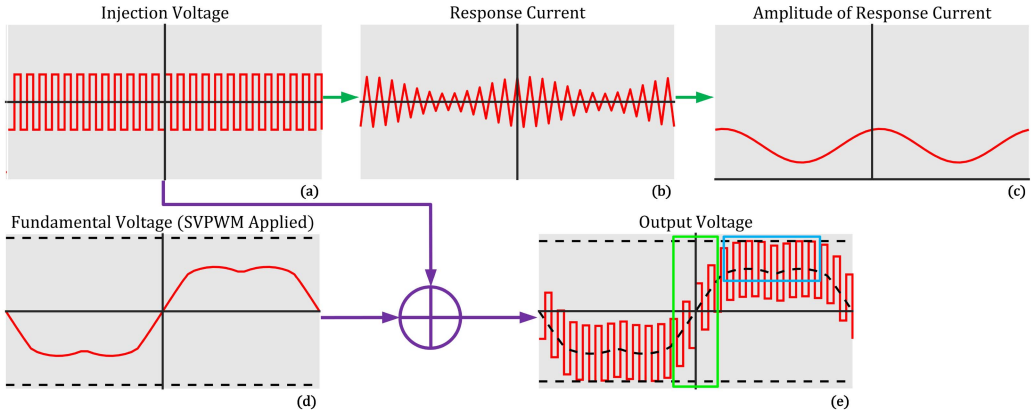

Fig. 2. Schematic of the conventional signal injection method.

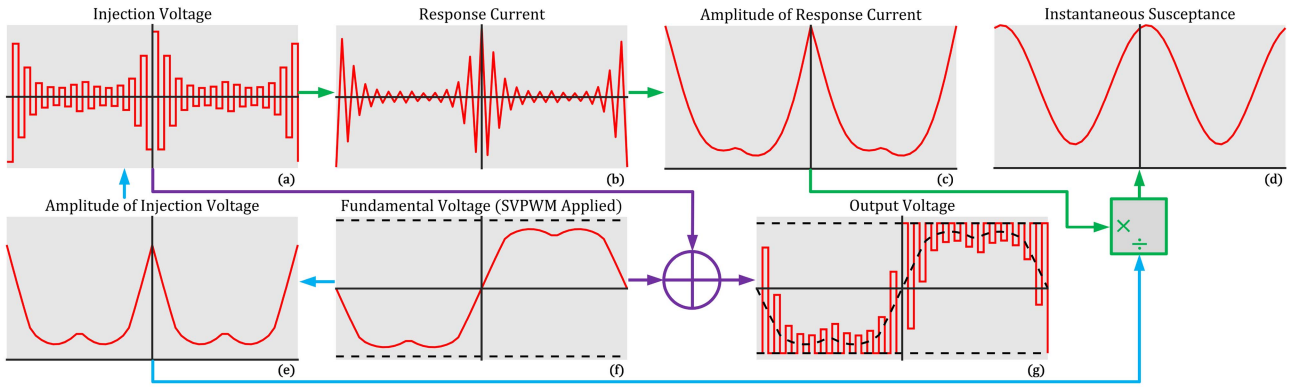

Fig. 3. Schematic of the proposed signal injection for susceptance extraction.

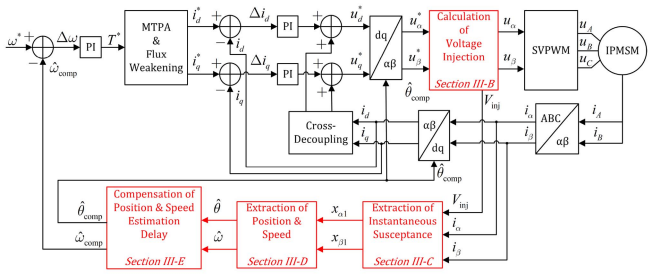

Fig. 4. Schematic diagram of the proposed sensorless control system.

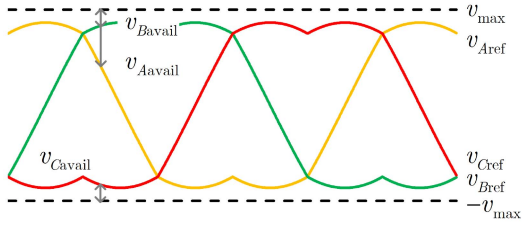

Fig. 5. Schematic diagram of available injection voltage for ABC phases.

The detailed implementation of the proposed method in Fig. 3 will be explained in the following subsections: calculation of injection voltage, extraction of instantaneous susceptance, extraction of position and speed information, and compensation of position and speed delay, corresponding to the red blocks in Fig. 4.

B. Calculation of Injection Voltage

This subsection presents the implementation of calculating the amplitude of the injection voltage [see Fig. 2(e)] based on the fundamental voltage [see Fig. 2(f)].

Given that the high-frequency signal period is sufficiently short, the fundamental voltage, which is the reference voltage provided by the current loop, is assumed constant within a period of the high-frequency injection voltage, so as the rotor position.

The reference voltages of the ABC phases with space vector pulse width modulation (SVPWM) applied are v_{Aref}, v_{Bref}, v_{Cref}, as shown in Fig. 5. Since the injection voltage must have equal positive and negative amplitudes, the available voltage for injecting high-frequency signals in each phase is evaluated separately for both positive and negative amplitudes. The available voltages for the ABC phases, shown in Fig. 5, are

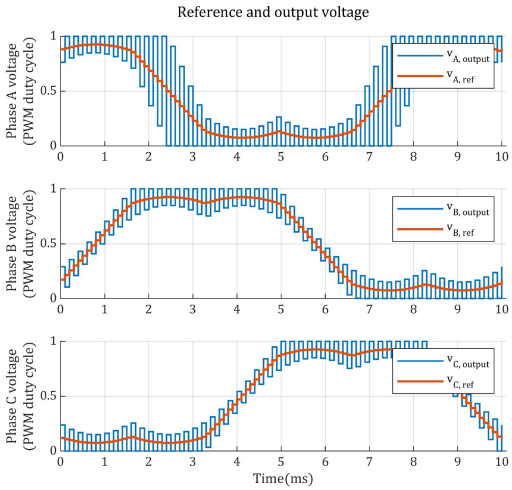

Fig. 6. Schematic of reference and proposed output voltage of ABC phases.

given as follows:

$$\begin{cases} v_{A\text{avail}} = \min(v_{\max} - v_{A\text{ref}}, v_{\max} + v_{A\text{ref}}) \\ v_{B\text{avail}} = \min(v_{\max} - v_{B\text{ref}}, v_{\max} + v_{B\text{ref}}) \\ v_{C\text{avail}} = \min(v_{\max} - v_{C\text{ref}}, v_{\max} + v_{C\text{ref}}) \end{cases} \tag{10}$$

where $v_{\max}$ denotes the maximum available voltage per phase, which can be set to $v_{\max} = v_{\text{DC}}/2$ in practical systems, where v_{DC} is the dc-bus voltage.

At low-speed conditions, the amplitude of the fundamental voltage is low, and a lower value can be selected for $v_{\max}$. As a typical selection, $v_{\max}$ is given as

$$v_{\max} = \max\left(0.5\frac{v_{\text{DC}}}{2}, \sqrt{v_d^2 + v_q^2} + 0.05\frac{v_{\text{DC}}}{2}\right). \tag{11}$$

To inject voltage on the α-axis while ensuring no injection component on the β-axis, the injection voltages of B and C phases must be equal. As a result, the injection voltage amplitudes of the three phases are given as

$$\begin{cases} v_{A\text{inj}} = v_{A\text{avail}} \\ v_{B\text{inj}} = v_{C\text{inj}} = -\min(v_{B\text{avail}}, v_{C\text{avail}}). \end{cases} \tag{12}$$

The amplitude of injection voltage on the α-axis is determined as

$$V_{\text{inj}} = v_{A\text{avail}} + \min(v_{B\text{avail}}, v_{C\text{avail}}). \tag{13}$$

Fig. 6 shows the typical three-phase voltage waveform of the proposed method with a fundamental voltage of the peak-to-peak amplitude of 85% pulse width modulation (PWM) duty cycle.

C. Extraction of Instantaneous Susceptance

This subsection implements the process of extracting the amplitude [see Fig. 3(c)] from the response current [see Fig. 3(b)] and obtaining the inductance information [as susceptance in Fig. 3(d)].

The procedures of voltage injection and response current demodulation are illustrated in Section II-B. In the equation of

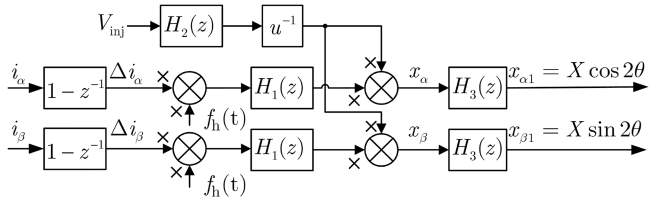

Fig. 7. Schematic diagram of the control system with filtering and demodulating system.

response current amplitude (7), the amplitude I_{inj} is proportional to that of the injection voltage V_{inj}. If the current amplitude I_{inj} is divided by the amplitude of the injection voltage V_{inj}, the influence of variation of the voltage amplitude can be eliminated, thereby making the demodulated signal dependent only on the rotor position.

The *instantaneous susceptance* is defined as the amplitude ratio of the response current (6) and (9) to the injection voltage (4) at the same instant, shown in (14). It characterizes the current variation induced by applying a unit voltage within one sampling period. While its definition is similar to the magnitude of susceptance, it does not represent the result under sinusoidal steady-state conditions but shares the same unit Ω^{-1}. The α-axis instantaneous susceptance is a sinusoidal signal superposed on a dc component, while the β-axis instantaneous susceptance is a sinusoidal signal with the same amplitude as the α-axis signal but phase-shifted by 90°. Both signals exhibit a frequency equal to twice the angular frequency of the rotor.

$$\begin{cases} x_\alpha = \frac{i_{\alpha\text{res}}}{V_{\text{inj}}} = T_{\text{s}}\left(\frac{1}{L_{\text{S}}} + \frac{1}{L_{\text{D}}}\cos 2\theta\right) \\ x_\beta = \frac{i_{\beta\text{res}}}{V_{\text{inj}}} = T_{\text{s}}\frac{1}{L_{\text{D}}}\sin 2\theta \end{cases} \tag{14}$$

To obtain the instantaneous susceptance according to its definition, it is necessary to acquire synchronized instantaneous values of both $i_{\alpha\text{res}}, i_{\beta\text{res}}$ and V_{inj} at each sample. For this purpose, a demodulation scheme, shown in Fig. 7, is specifically designed to extract the amplitudes of response currents while maintaining strict synchronization with the amplitude of injection voltage.

The increments of α- and β-axes currents $\Delta i_\alpha, \Delta i_\beta$ are multiplied by the carrier signal $f_{\text{h}}(t)$, and passed through a low-pass filter (15) to obtain the demodulated currents.

$$H_1(z) = \left(\frac{1 + z^{-1}}{2}\right)^{k_{\text{LPF}}} \tag{15}$$

where z^{-1} is the discrete-time unit delay operator. k_{LPF} is the filter order, and $k_{\text{LPF}} = 3$ is taken in this article.

The amplitude of injection voltage V_{inj} should pass through the same low-pass filter to obtain the same phase delay. Also, a one-sample delay on the application of voltage is introduced by the structure of converters, so an additional unit delay compensation is required. The compensation for the high-frequency voltage amplitude signal is as follows:

$$H_2(z) = z^{-1}H_1(z). \tag{16}$$

TABLE II
EKF VARIABLES AND DEFINITIONS

Symbol	Definition	Dimension
$\boldsymbol{x}$	State vector	$\mathbb{R}^3$
$\boldsymbol{u}$	System input measurement vector	$\mathbb{R}^2$
$\boldsymbol{F}$	State transition matrix	$\mathbb{R}^{3\times3}$
$\boldsymbol{h}(\boldsymbol{x})$	Nonlinear measurement function	$\mathbb{R}^2$
$\boldsymbol{H}(\boldsymbol{x})$	Measurement Jacobian matrix	$\mathbb{R}^{2\times3}$
$\boldsymbol{Q}$	Process uncertainty matrix	$\mathbb{R}^{3\times3}$
$\boldsymbol{R}$	Measurement uncertainty matrix	$\mathbb{R}^{2\times2}$
$\hat{\boldsymbol{x}}$	Estimated state vector	$\mathbb{R}^3$
$\hat{\boldsymbol{P}}$	State uncertainty matrix	$\mathbb{R}^{3\times3}$
$\boldsymbol{K}$	Kalman gain matrix	$\mathbb{R}^{3\times2}$
k	Number of iterations	$\mathbb{N}$
A	Signal amplitude	$\mathbb{R}$
θ	Rotor position	$\mathbb{R}$
ω	Rotor speed	$\mathbb{R}$
q_ω	Variance of rotor speed	$\mathbb{R}$
$r_{x\alpha}, r_{x\beta}$	Measurement noise variance of $x_{\alpha1}$ and $x_{\beta1}$	$\mathbb{R}$

The instantaneous susceptance on the α- and β-axes are obtained by passing the amplitude of the injection voltage through a division operator u^{-1} and multiplying it with the demodulated current signal, as shown in Fig. 7.

The α-axis instantaneous susceptance contains a dc component, illustrated in (14), which can be filtered out by a high-pass filter with a very low cut-off frequency. The β-axis instantaneous susceptance may also contain a dc component in actual systems due to nonideal factors, which can be filtered out by the same high-pass filter. The filtered instantaneous susceptance $x_{\alpha1}$ and $x_{\beta1}$ are shown as follows:

$$x_{\alpha1} = \mathrm{HPF}(x_\alpha) \quad x_{\beta1} = \mathrm{HPF}(x_\beta) \tag{17}$$

where the high-pass filter is implemented as a second-order Butterworth filter (18), in which ζ is the damping ratio and ω_3 is the characteristic frequency.

$$H_3(z) = \frac{2\zeta\omega_3 T_\mathrm{s}(1-z^{-1})}{(1+2\zeta\omega_3 T_\mathrm{s}+\omega_3^2 T_\mathrm{s}^2)-2(1+\zeta\omega_3 T_\mathrm{s})z^{-1}+z^{-2}}. \tag{18}$$

D. Extraction of Position and Speed Information

In this subsection, the rotor position is extracted from the instantaneous susceptance signal [see Fig. 3(d)].

An extended Kalman filter (EKF) is used to extract rotor position from the filtered instantaneous susceptance $x_{\alpha1}$ and $x_{\beta1}$, which are orthogonal sinusoidal signals, and to obtain the estimation of rotor position $\hat{\theta}$ and rotor speed $\hat{\omega}$. The variables used in the EKF are listed in Table II.

The state vector $\boldsymbol{x}$, the system input measurement vector $\boldsymbol{u}$, the state transition matrix $\boldsymbol{F}$, the nonlinear measurement function $\boldsymbol{h}(\boldsymbol{x})$ and its Jacobian matrix $\boldsymbol{H}(\boldsymbol{x})$, the process uncertainty matrix $\boldsymbol{Q}$, and measurement uncertainty matrix $\boldsymbol{R}$ are given as follows:

$$\boldsymbol{x} = \begin{bmatrix} A \\ \theta \\ \omega \end{bmatrix}, \ \boldsymbol{u} = \begin{bmatrix} x_{\alpha1} \\ x_{\beta1} \end{bmatrix}, \ \boldsymbol{F} = \begin{bmatrix} 1 & 0 & 0 \\ 0 & 1 & T_\mathrm{s} \\ 0 & 0 & 1 \end{bmatrix}$$

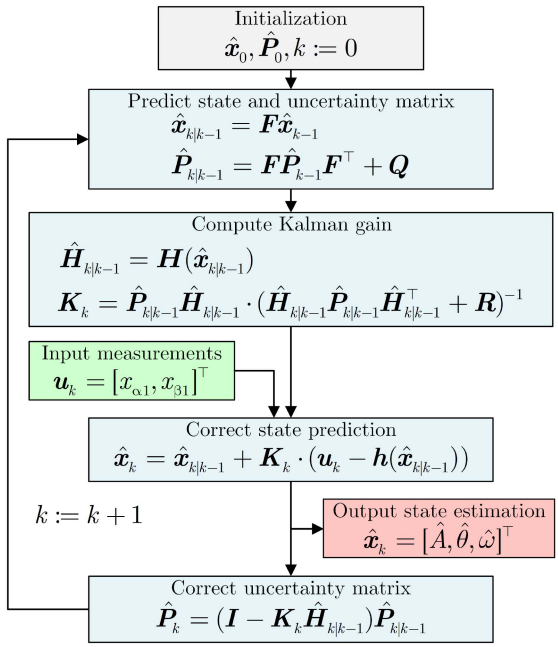

Fig. 8. Schematic diagram of the EKF for rotor position and speed extraction.

$$\boldsymbol{h}(\boldsymbol{x}) = \begin{bmatrix} A\sin(2\theta) \\ A\cos(2\theta) \end{bmatrix}, \boldsymbol{H}(\boldsymbol{x}) = \begin{bmatrix} \sin(2\theta) & 2A\cos(2\theta) & 0 \\ \cos(2\theta) & -2A\sin(2\theta) & 0 \end{bmatrix}$$

$$\boldsymbol{Q} = \begin{bmatrix} 0 & 0 & 0 \\ 0 & 0 & 0 \\ 0 & 0 & q_\omega \end{bmatrix}, \ \boldsymbol{R} = \begin{bmatrix} r_{x\alpha} & 0 \\ 0 & r_{x\beta} \end{bmatrix}.$$

The EKF algorithm is detailed in Fig. 8, which is adapted from [26] following a similar structure. The first step is the initialization of the estimation of the state vector $\hat{\boldsymbol{x}}_0$ and its uncertainty matrix $\hat{\boldsymbol{P}}_0$, which is performed only before the first iteration. Then, the prediction stage is computed based on the previous estimation, obtaining $\hat{\boldsymbol{x}}_{k|k-1}$ and $\hat{\boldsymbol{P}}_{k|k-1}$. With $\hat{\boldsymbol{P}}_{k|k-1}$ and the measurement Jacobian matrix $\hat{\boldsymbol{H}}_{k|k-1}$, the Kalman gain $\boldsymbol{K}_k$ is computed. Then, the correction of the state prediction is performed with the error between the input measurement $\boldsymbol{u}_k$ and the predicted measurement $\boldsymbol{h}(\hat{\boldsymbol{x}}_{k|k-1})$. Finally, the uncertainty matrix $\hat{\boldsymbol{P}}_k$ is corrected, and the algorithm repeats until the end of the operation.

E. Compensation for Position and Speed Estimation Delay

Delay in estimated position and speed signals is introduced during both the demodulation of high-frequency currents and the estimation process of the EKF. A compensation system is implemented for the delay, shown in Fig. 9. The EKF-estimated speed of $\hat{\omega}$ is passed through a bandwidth-limited differentiator (19) with a bandwidth of ω_deri to obtain its variation rate $\mathrm{d}\hat{\omega}/\mathrm{d}t$. The compensated position $\hat{\theta}_\mathrm{comp}$ and speed $\hat{\omega}_\mathrm{comp}$ are shown in (20) and (21), which are the final results of position estimation

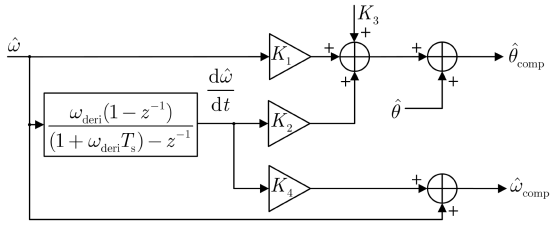

Fig. 9. Schematic diagram of the position and speed-delay compensation system.

TABLE III
PARAMETERS OF MOTOR IN SIMULATION

Symbol	Definition	Value
L_d	d-axis inductance	1.0 mH
L_q	q-axis inductance	1.5 mH
R_s	stator resistance	0.4 Ω
ψ	permanent magnet flux linkage	0.02 Wb
n_p	number of pole pairs	2
I_N	rated phase current	7 A
V_N	rated line voltage	24.5 V
P_N	rated power	220 W
T_N	rated torque	0.55 Nm
f_N	rated frequency	130 Hz
J	moment of inertia of rotor	0.001 kg · m^2

process.

$$H_{\text{deri}}(z) = \frac{\omega_{\text{deri}}(1-z^{-1})}{(1+\omega_{\text{deri}}T_s)-z^{-1}} \tag{19}$$

$$\hat{\theta}_{\text{comp}} = \hat{\theta} + K_1\hat{\omega} + K_2\frac{d\hat{\omega}}{dt} + K_3 \tag{20}$$

$$\hat{\omega}_{\text{comp}} = \hat{\omega} + K_4\frac{d\hat{\omega}}{dt}. \tag{21}$$

The coefficients K_1, K_2, and K_3 for position compensation, and the coefficient K_4 for speed compensation, are calibrated as follows. By operating the position estimation system in open-loop mode within the simulation environment, comprehensive data are collected, including position and speed estimation errors, estimated speed $\hat{\omega}$, and its variation rate $d\hat{\omega}/dt$. Optimal compensation coefficients are obtained with a multivariable linear regression analysis on the collected data.

IV. SIMULATION RESULTS

In this section, a simulation of open-loop position estimation based on the proposed method is conducted. The simulations consist of two parts. The first part is designed to demonstrate the principle of the proposed method, while the second part is to validate the necessity and effectiveness of the voltage amplitude signal delay compensation, which is conducted as (16).

The motor parameters used in the simulation are presented in Table III, while the controller parameters are listed in Table IV.

A. Simulation 1

The simulation is conducted with ideal current sampling, under the rated speed with 80% of the rated load. The difference between the maximum value of the output voltage and that of the reference voltage is 2.5% of the dc-bus voltage, shown in Fig. 10, which means a 5% occupancy of the dc-bus voltage as shown in Fig. 11. In the following discussion, this condition of the injection voltage will be described as *occupying 5% of the dc-bus voltage*.

Due to the variation of the amplitude of the injection voltage, the waveform of the response current is not a sinusoidal wave, as shown in Fig. 12. The instantaneous susceptance waveform presents as a distortion-free orthogonal sinusoidal signal, as Fig. 13. As observed in Fig. 13, the EKF-estimated instantaneous

TABLE IV
PARAMETERS OF CONTROLLER IN SIMULATION

Symbol	Definition	Value
f_{sw}	switching frequency	5 kHz
f_s	sampling frequency	10 kHz
v_{DC}	DC-bus voltage	35 V

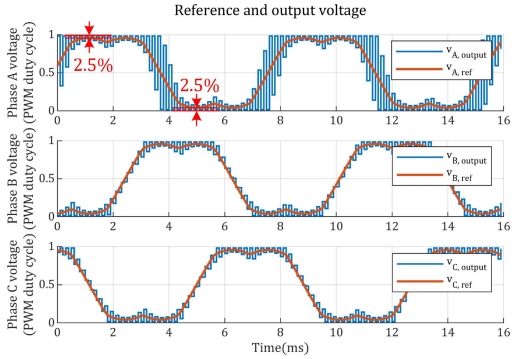

Fig. 10. Simulation 1: Reference and output voltage of ABC phases.

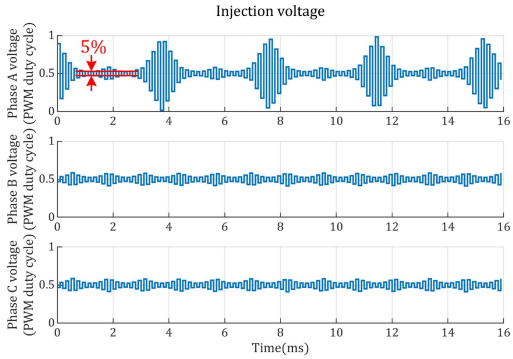

Fig. 11. Simulation 1: Injection voltage of ABC phases.

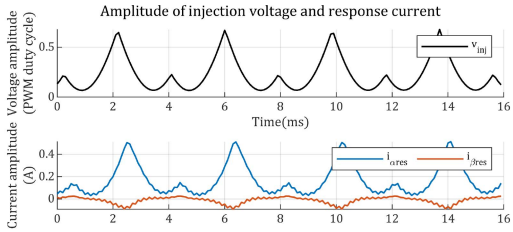

Fig. 12. Simulation 1: Amplitude of injection voltage and response current.

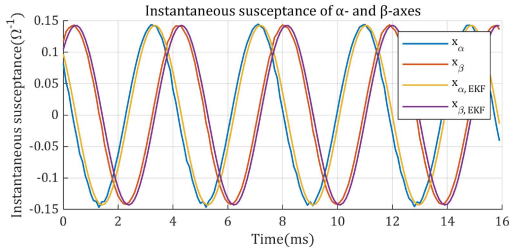

Fig. 13. Simulation 1: Instantaneous susceptance of α- and β-axes.

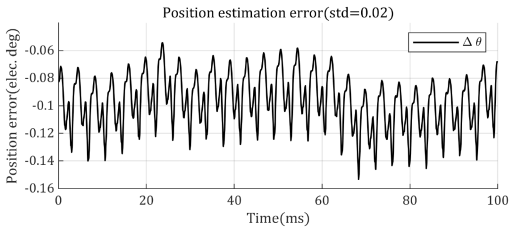

Fig. 14. Simulation 1: Position estimation error.

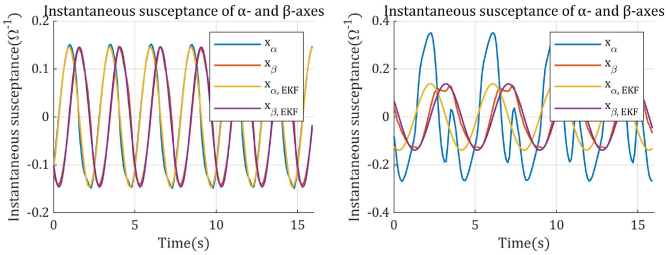

Fig. 15. Simulation 2: Instantaneous susceptance of α- and β-axes. (a) Voltage delay compensated. (b) Voltage delay not compensated.

susceptance exhibits phase delay relative to the actual value due to its inherent limitation in tracking sinusoidal signals. The phase delay presents as a dc offset in the position estimation, which is eliminated by compensation in Section III-E. As a result, the position estimation error shown in Fig. 14 is low.

B. Simulation 2

The simulation is conducted with 5% dc-bus voltage occupancy, under 200% of the rated speed with 40% of the rated load. Contrast simulations are performed for both cases: with and without voltage compensation, which is conducted as (16). A higher rotational speed is employed in the simulations to amplify the effects of voltage delay compensation errors.

As shown in Fig. 15, significant distortion is introduced into the instantaneous susceptance waveform if the voltage delay is not compensated. Periodic errors in position estimation results are introduced by the absent voltage compensation, shown in Fig. 16.

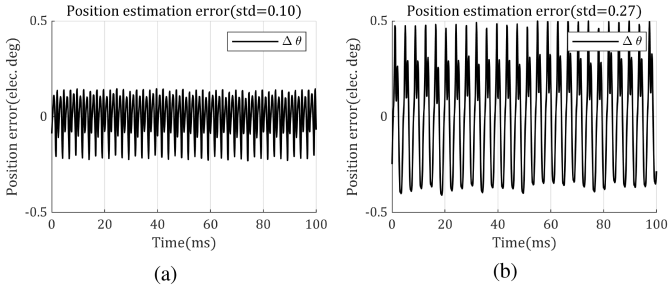

Fig. 16. Simulation 2: Position estimation error. (a) Voltage delay compensated. (b) Voltage delay not compensated.

TABLE V
PARAMETERS OF MOTOR IN EXPERIMENT

Symbol	Definition	Value
L_d	d-axis inductance	1.947 mH
L_q	q-axis inductance	2.871 mH
R_s	stator resistance	1.601 Ω
ψ	permanent magnet flux linkage	0.02115 Wb
n_p	number of pole pairs	3
I_N	rated phase current	4.2 A
V_N	rated line voltage	20.8 V
P_N	rated power	80 W
T_N	rated torque	0.4 Nm
f_N	rated frequency	100 Hz

TABLE VI
PARAMETERS OF CONTROLLER IN EXPERIMENT

Symbol	Definition	Value
f_{sw}	switching frequency	10 kHz
f_s	sampling frequency	10 kHz
v_{DC}	DC-bus voltage	35 V
i_{LSB}	Current sampling resolution	7.32 mA

V. EXPERIMENT RESULTS

This section presents experimental validation of the control system with the proposed signal injection method. The tests are divided into two parts. The first part follows procedures similar to the simulation in Section IV to demonstrate the principles of the proposed method. The second part employs closed-loop control experiments to verify the performance of the proposed method in closed-loop systems.

The motor parameters used in the experiment are presented in Table V, while the controller parameters are listed in Table VI. The motor control platform employed in the experimental tests is shown in Fig. 17.

A. Open-Loop Estimation Experiment

In this section, two sets of tests are conducted. The first test performs open-loop estimation experiments for the proposed signal injection method. The second test validates the necessity and effectiveness of the voltage amplitude signal delay compensation, which is conducted as (16).

1) Test 1: Test 1 is conducted under the rated speed with 50% of the rated load.

The injection voltage occupies 14% of the dc-bus voltage, shown in Fig. 18.

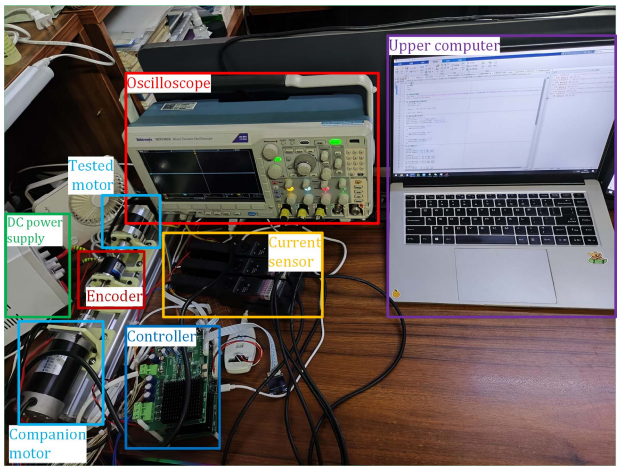

Fig. 17. Photograph of the motor control platform.

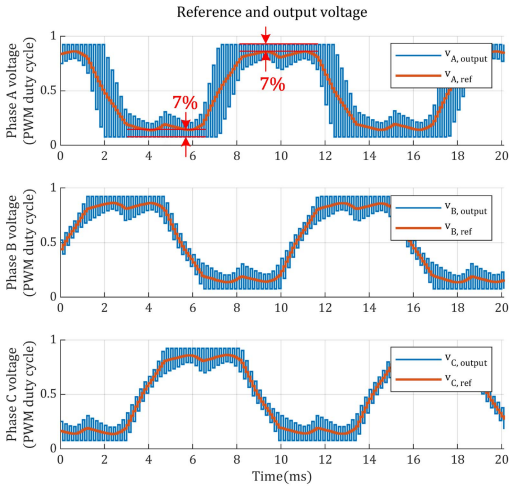

Fig. 18. Test 1: Reference and output voltage of ABC phases.

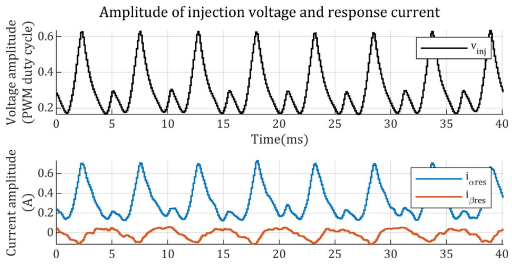

Fig. 19. Test 1: Amplitude of injection voltage and response current.

Fig. 19 presents the amplitude of injection voltage and the α- and β-axes response currents under loaded conditions. Due to the variation of amplitude of injection voltage, the waveforms of response current are not sinusoidal waves, as shown in Fig. 19. A strict synchronization between the peak positions of both the amplitude of injection voltage and the α-axes response current is observed, which validates the effectiveness of the voltage amplitude signal delay compensation.

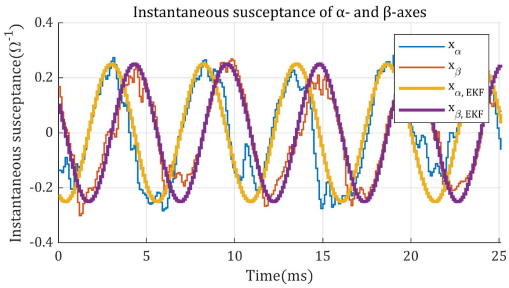

Fig. 20. Test 1: Instantaneous susceptance of α- and β-axes.

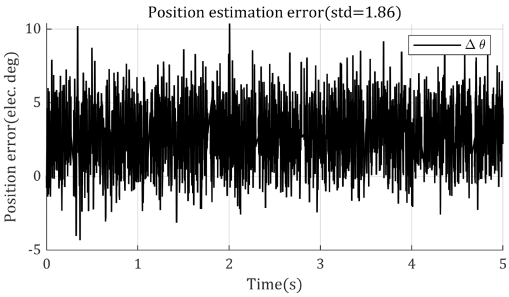

Fig. 21. Test 1: Position estimation error.

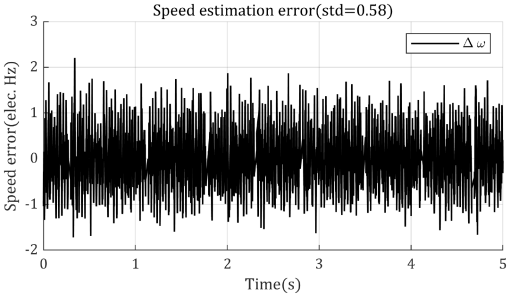

Fig. 22. Test 1: Speed estimation error.

The waveforms of instantaneous susceptance of α- and β-axes appear as orthogonal sinusoidal signals, represented by the thinner lines in Fig. 20. The EKF method successfully extracts the fundamental component, shown as the thicker lines in the figure.

The estimated position and speed of the EKF are compared with encoder measurements. The corresponding position and speed errors are shown in Figs. 21 and 22.

2) Test 2: Test 2 is conducted at the rated speed with 50% of the rated load, with the injection voltage occupying 5% of the dc-bus voltage, while the voltage delay compensation in (16) is removed.

As shown in Fig. 23, distortion is introduced into the waveform of the instantaneous susceptance if the voltage delay is not compensated. The absence of compensation introduces an offset in the position estimation results, shown in Fig. 24. Compared

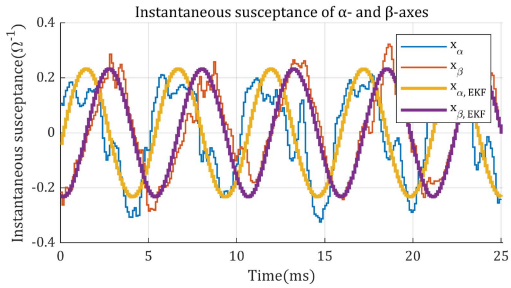

Fig. 23. Test 2: Instantaneous susceptance of α- and β-axes without voltage delay compensation.

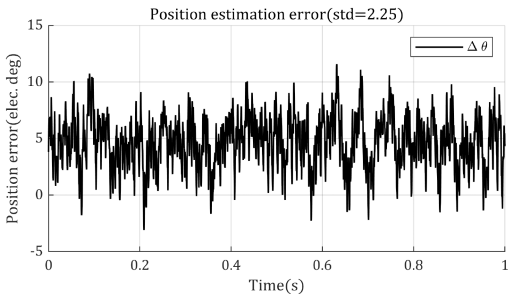

Fig. 24. Test 2: Position estimation error without voltage delay compensation.

to simulation results in Section IV-B, the distortion of instantaneous susceptance decreases because of the lower speed in the experiment.

B. Closed-Loop Control Experiment

In this section, closed-loop control experiments are conducted. Two sets of tests are performed separately. The first test applies rated torque at rated speed, while the second test applies 40% of rated load at 200% of rated speed. Since the proposed algorithm is only suitable for medium-to-high speed ranges, the proposed position estimation algorithm is switched in loop at 50% rated speed.

1) Test 3: In this test, a rated load is applied at rated speed and removed soon.

A load is applied at $t = 9$ s, and then, removed at $t = 17$ s. Fig. 25 presents a comparison between the estimated speed and the actual speed, which is obtained from the encoder, during the whole test process.

Fig. 26 presents a comparison between the estimated speed and the actual speed during the acceleration process. No time lag is observed between the estimated speed and the actual speed, which meets the bandwidth requirements for the speed control loop.

The sampled currents of the oscilloscope reveal the waveform of response current induced by the injection voltage, shown in the red-boxed regions in Fig. 27. These response currents manifest as triangular waveforms superposed on the fundamental current. While the amplitude of triangular waveforms varies within one fundamental period, it exhibits identical amplitude variation patterns across different fundamental periods.

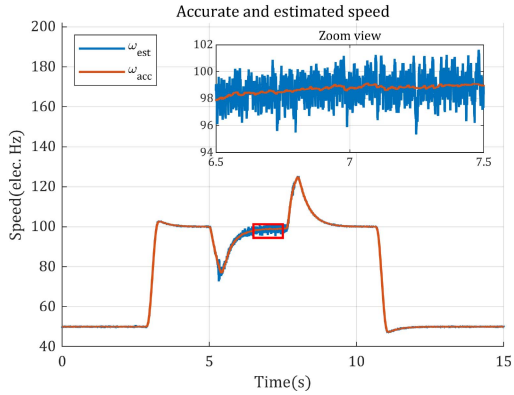

Fig. 25. Test 3: Speed during the whole test process.

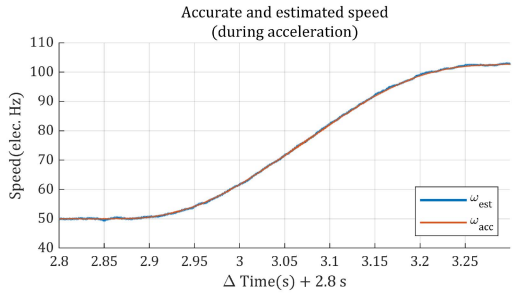

Fig. 26. Test 3: Speed during acceleration process.

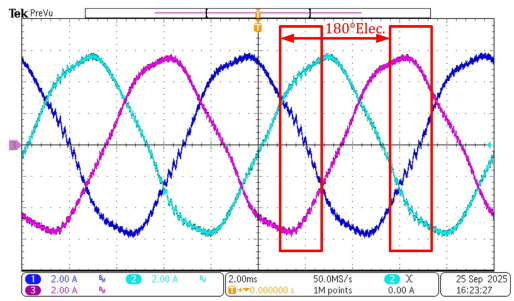

Fig. 27. Test 3: ABC-phase current waveforms under rated load at rated speed.

Fig. 28 presents the d- and q-axes currents throughout the entire experimental process. The zoomed region displays the d- and q-axes currents under rated conditions. The torque controller employs a fixed current angle strategy for d- and q-axes reference currents, which leads to the nonzero d-axis current. The current ripples originate from the harmonic components of the back EMF, which are uncompensated in the control scheme.

Fig. 29 presents the d- and q-axes voltages throughout the entire experimental process. The zoomed region shows the d- and q-axes voltages under rated conditions. Under rated conditions, the d-axis voltage approaches the maximum output voltage, and the dc-bus voltage is fully utilized by the fundamental voltage.

Fig. 30 presents the reference and output voltages. The figure clearly shows the injection voltage occupying 5% of the dc-bus voltage, observed at the peaks of the waveform of the reference

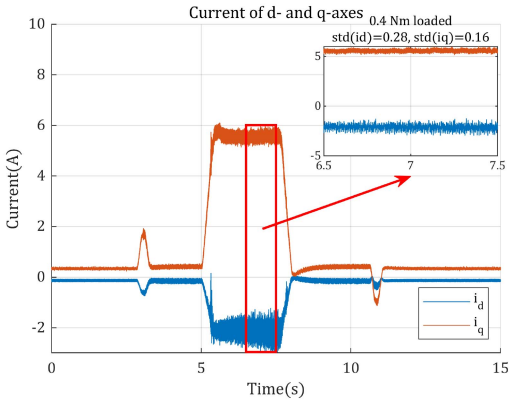

Fig. 28. Test 3: d- and q-axes current during the whole test process.

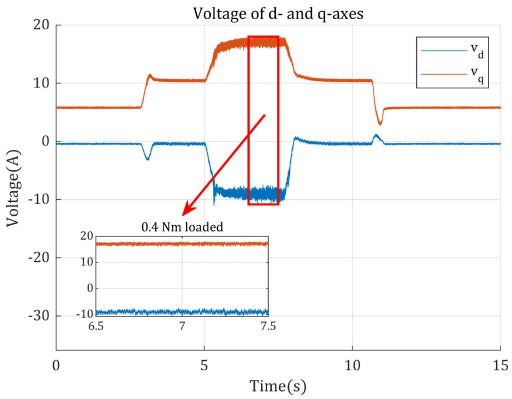

Fig. 29. Test 3: d- and q-axes voltage during the whole test process.

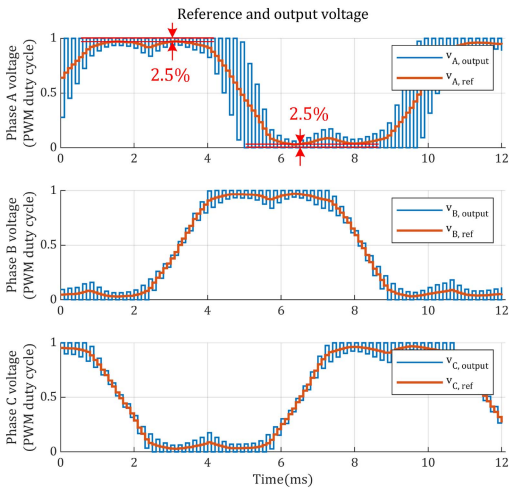

Fig. 30. Test 3: Reference and output voltage at rated condition.

voltages. During the test, the motor operates under rated conditions, exhibiting slight saturation that creates a flat-top in the voltage waveforms.

Fig. 31 displays the instantaneous susceptance under rated conditions along with the EKF filtered results. Noise is observed in the waveforms of instantaneous susceptance, with relatively

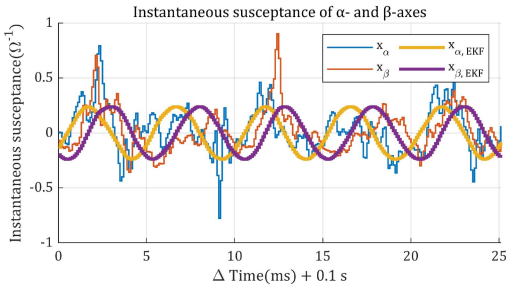

Fig. 31. Test 3: Instantaneous susceptance of α- and β-axes.

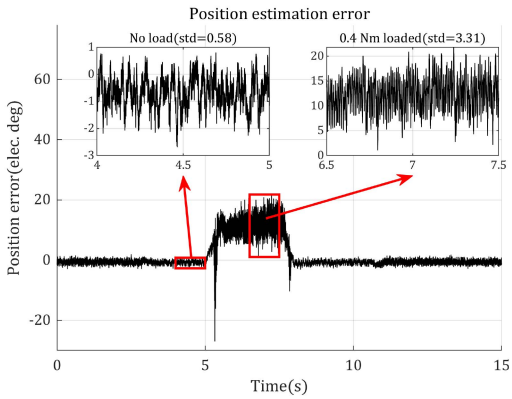

Fig. 32. Test 3: Position estimation error during the whole test process.

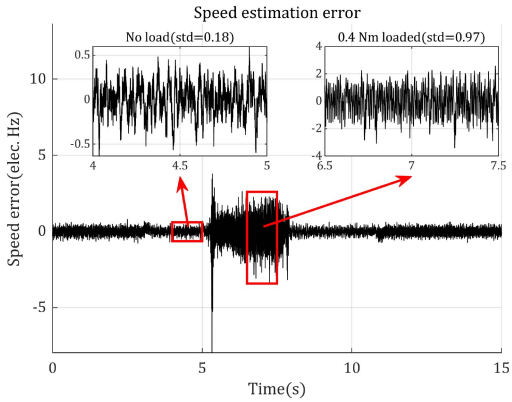

Fig. 33. Test 3: Speed estimation error during the whole test process.

higher noise levels at the peaks of the sinusoidal waveforms, which corresponds to the noise amplification effect of the division operation to obtain instantaneous susceptance.

Figs. 32 and 33 present the estimated position and speed errors, respectively. The main regions display the errors throughout the entire experimental process, while the zoomed regions show the errors under rated conditions. As observed in both figures, when load is applied to the motor, the standard deviations of both position and speed errors increase relatively as the injection voltage is limited. The estimated position exhibits an offset when high load torque is applied, which is similar to

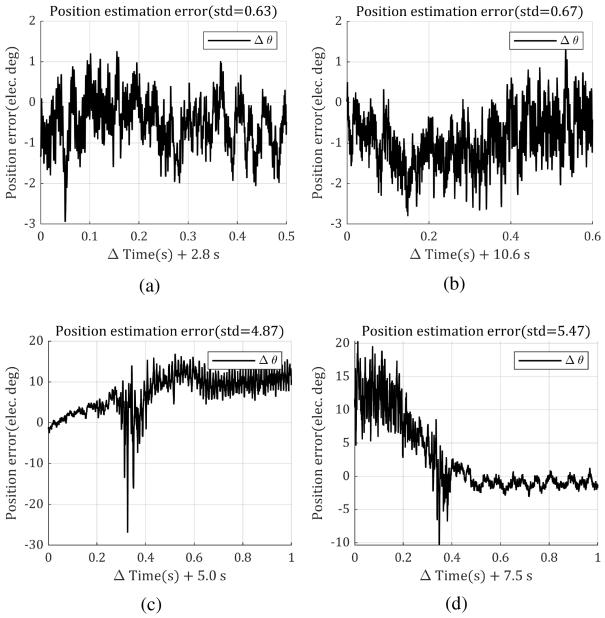

Fig. 34. Test 3: Position error during transient process. (a) Accelerating. (b) Decelerating. (c) Load applying. (d) Load removing.

reported results in [20] and [24], and can be compensated in the control scheme without control performance debasement.

Fig. 34 illustrates the position estimation error during transient processes. The corresponding operating conditions include acceleration from 50 to 100 Hz, deceleration from 100 to 50 Hz, application of rated load, and removal of rated load. As observed in Fig. 34(a) and (b), no significant impulse in the position estimation error is present during the acceleration and deceleration processes. However, during the load application process, as shown in Fig. 34(c), a brief impulse in the position estimation error occurs when the load increases to the rated value, but it quickly recovers to the steady state. During load removal, as depicted in Fig. 34(d), the position estimation error varies smoothly with the decrease in load, without any observable impulse.

2) Test 4: In this test, 37% of the rated load (0.15 Nm) is applied at 200% of the rated speed and removed soon.

The load is applied at t=14.5 s, and then, removed at t=19 s. Fig. 35 compares the estimated speed with the actual speed, which is obtained by the encoder. During the test, the motor operates exceeding the rated speed, resulting in output power below the rated power.

The response currents of the injection voltage are observed in the sampled currents of the oscilloscope, shown in red-boxed regions in Fig. 36. Compared to that under the rated condition in Fig. 27, the triangular-waved response currents have higher amplitudes and are more clearly observed in Fig. 36, as the position of the injection voltage shifts closer to the d-axis, where the inductance is lower.

Fig. 37 presents the waveforms of the reference and output voltages. The injection voltage occupies 5% of the dc-bus voltage, observed as the 2.5% difference of dc-bus voltage between the maximum values of the reference and output voltages.

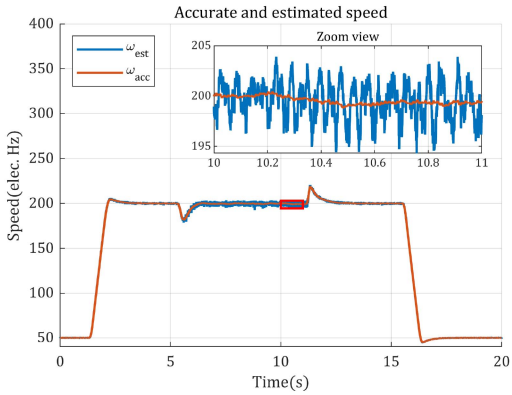

Fig. 35. Test 4: Speed during the whole test process.

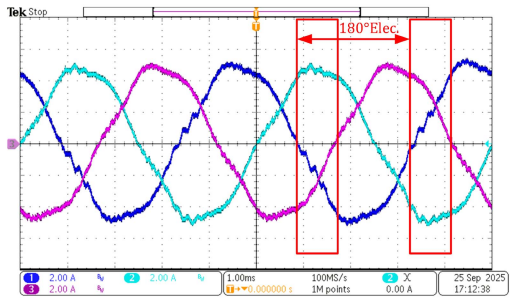

Fig. 36. Test 4: ABC-phase current waveforms under 25% of rated load at 200% of rated speed.

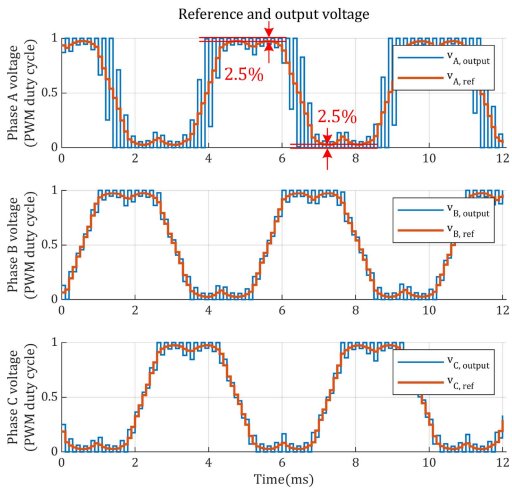

Fig. 37. Test 4: Reference and output voltage at loaded condition.

Fig. 38 displays the instantaneous susceptance under loaded conditions along with the EKF-filtered results. Figs. 39 and 40 present the estimated position and speed errors, respectively. In comparison with the results at rated condition in Figs. 31–33, the increment of motor speed shows no negative effect on the position estimation.

Fig. 41 presents the variation curves of the position estimation error during transient processes. The corresponding operating

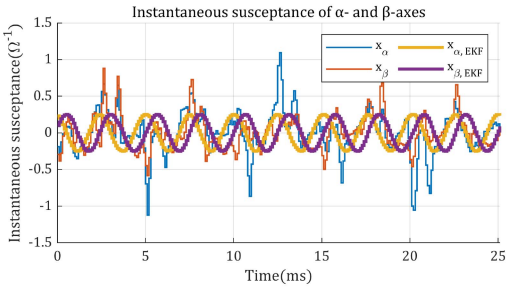

Fig. 38. Test 4: Instantaneous susceptance of α- and β-axes.

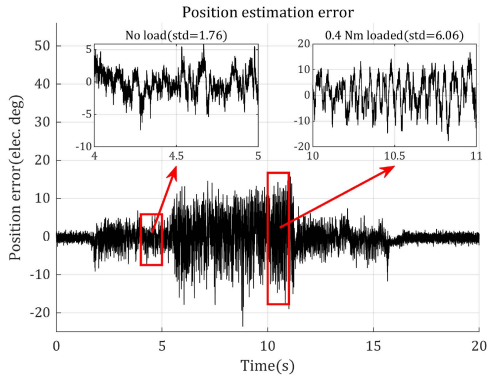

Fig. 39. Test 4: Position estimation error during the whole test process.

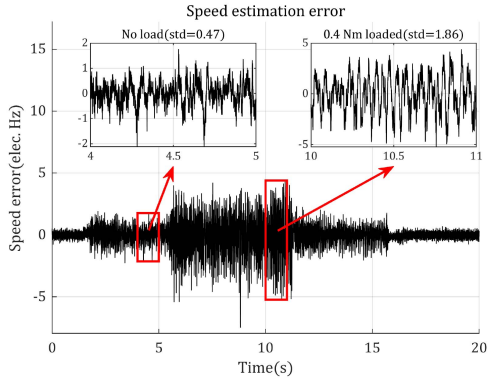

Fig. 40. Test 4: Speed estimation error during the whole test process.

conditions include acceleration from 50 to 200 Hz, deceleration from 200 to 50 Hz, application of a 0.15-Nm load, and removal of the load. None of the processes shown in Fig. 41 exhibit significant impulses. The estimation error varies smoothly in response to changes in operating conditions.

The experimental results in Sections V-B1 and V-B2 demonstrate the effectiveness of the proposed method at both rated speed and exceeding rated speed with low dc-bus voltage occupancy. Furthermore, closed-loop control tests exceeding the rated speed confirm that the proposed method can extend the operating range of signal injection sensorless methods to voltage-constrained conditions. In terms of speed and position estimation errors, the proposed method achieves performance comparable to conventional model-based methods, thereby validating the effectiveness of the proposed method.

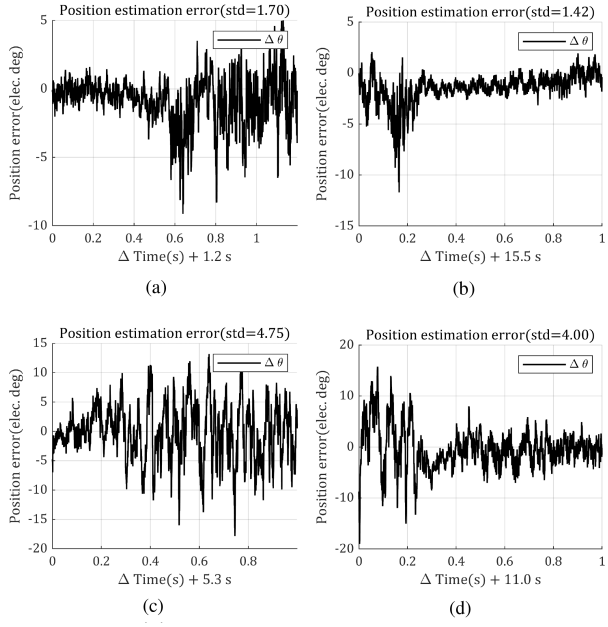

Fig. 41. Test 4: Position error during transient process. (a) Accelerating. (b) Decelerating. (c) Load applying. (d) Load removing.

C. Comparison of DC-Bus Voltage Occupancy

To evaluate the superiority of the proposed method in terms of voltage utilization, the achieved dc-bus voltage occupancy ratio of 5% is compared with various signal injection methods reported in the literature, as summarized in Table I. Conventional methods, including both square-wave and sinusoidal injection, typically exhibit high occupancy ratios (ranging from 22.7% to 71%). The method in [21] achieves a relatively low ratio of 7.44%, but it uses a much lower injection frequency (500 Hz), resulting in significant torque pulsations and system instability. In contrast, the proposed variable amplitude pulsating signal injection method maintains a high injection frequency (5 kHz) while occupying only 5% of the dc-bus voltage, representing a substantial improvement. This enhancement not only extends the operational speed range of signal injection-based sensorless control but also reduces the demand on the dc-bus voltage, thereby improving overall system performance.

VI. Conclusion

This article improves the sensorless control with pulsating signal injection in the SRF. A variable amplitude injection method is proposed, where the amplitude is computed from the fundamental three-phase output voltage and the dc-bus voltage. A high-frequency response current demodulation method for varying amplitude injection voltage is developed. The instantaneous susceptance is introduced to eliminate the influence of amplitude variation, and its sinusoidal-varying characteristic is revealed. An EKF-based method extracts rotor position from instantaneous susceptance. A position and speed-delay compensation system for estimation results is introduced to achieve low-latency estimation. The effectiveness of the proposed method in closed-loop control systems is validated through experiments.

The proposed method significantly improves dc-bus voltage utilization, thus reducing the dc-bus voltage occupancy ratio of injection voltage to merely 5%, which represents a great improvement compared with conventional methods, and extends the operational speed range of signal injection methods.

REFERENCES

[1] G. Wang, M. Valla, and J. Solsona, "Position sensorless permanent magnet synchronous machine drives—A review," *IEEE Trans. Ind. Electron.*, vol. 67, no. 7, pp. 5830–5842, Jul. 2020.

[2] G. Zhang, G. Wang, and D. Xu, "Saliency-based position sensorless control methods for PMSM drives—A review," *Chin. J. Elect. Eng.*, vol. 3, no. 2, pp. 14–23, Sep. 2017.

[3] S.-K. Sul, Y.-C. Kwon, and Y. Lee, "Sensorless control of IPMSM for last 10 years and next 5 years," *CES Trans. Elect. Mach. Syst.*, vol. 1, no. 2, pp. 91–99, 2017.

[4] A. Benevieri, A. Formentini, M. Marchesoni, M. Passalacqua, and L. Vaccaro, "Sensorless control with switching frequency square wave voltage injection for SPMSM with low rotor magnetic anisotropy," *IEEE Trans. Power Electron.*, vol. 38, no. 8, pp. 10060–10072, Aug. 2023.

[5] J. Lee, Y.-C. Kwon, and S.-K. Sul, "Signal-injection sensorless control with tilted current reference for heavily saturated IPMSMs," *IEEE Trans. Power Electron.*, vol. 35, no. 11, pp. 12100–12109, Nov. 2020.

[6] Y. Zhang, Z. Yin, J. Liu, R. Zhang, and X. Sun, "IPMSM sensorless control using high-frequency voltage injection method with random switching frequency for audible noise improvement," *IEEE Trans. Ind. Electron.*, vol. 67, no. 7, pp. 6019–6030, Jul. 2020.

[7] A. Yousefi-Talouki, P. Pescetto, G. Pellegrino, and I. Boldea, "Combined active flux and high-frequency injection methods for sensorless direct-flux vector control of synchronous reluctance machines," *IEEE Trans. Power Electron.*, vol. 33, no. 3, pp. 2447–2457, Mar. 2018.

[8] R. Ni, D. Xu, F. Blaabjerg, K. Lu, G. Wang, and G. Zhang, "Square-wave voltage injection algorithm for PMSM position sensorless control with high robustness to voltage errors," *IEEE Trans. Power Electron.*, vol. 32, no. 7, pp. 5425–5437, Jul. 2017.

[9] G. Wang, R. Yang, and D. Xu, "DSP-Based control of sensorless IPMSM drives for wide-speed-range operation," *IEEE Trans. Ind. Electron.*, vol. 60, no. 2, pp. 720–727, Feb. 2013.

[10] N. Bianchi, E. Fornasiero, and S. Bolognani, "Effect of stator and rotor saturation on sensorless rotor position detection," in *Proc. IEEE Energy Convers. Congr. Expo.*, Sep. 2011, pp. 1528–1535.

[11] Y.-D. Yoon, S.-K. Sul, S. Morimoto, and K. Ide, "High-bandwidth sensorless algorithm for AC machines based on square-wave-type voltage injection," *IEEE Trans. Ind. Appl.*, vol. 47, no. 3, pp. 1361–1370, May-Jun. 2011.

[12] J.-H. Jang, S.-K. Sul, J.-I. Ha, K. Ide, and M. Sawamura, "Sensorless drive of surface-mounted permanent-magnet motor by high-frequency signal injection based on magnetic saliency," *IEEE Trans. Ind. Appl.*, vol. 39, no. 4, pp. 1031–1039, Jul./Aug. 2003.

[13] M. Naderian, G. A. Markadeh, M. Karimi-Ghartemani, and M. Mojiri, "Improved sensorless control strategy for IPMSM using an ePLL approach with high-frequency injection," *IEEE Trans. Ind. Electron.*, vol. 71, no. 3, pp. 2231–2241, Mar. 2024.

[14] K. Yu and Z. Wang, "Position sensorless control of IPMSM using adjustable frequency setting square-wave voltage injection," *IEEE Trans. Power Electron.*, vol. 37, no. 11, pp. 12973–12979, Nov. 2022.

[15] D. Wen, W. Wang, and Y. Zhang, "Sensorless control of permanent magnet synchronous motor in full speed range," *Chin. J. Elect. Eng.*, vol. 8, no. 2, pp. 97–107, Jun. 2022.

[16] G. Wang, D. Xiao, G. Zhang, C. Li, X. Zhang, and D. Xu, "Sensorless control scheme of IPMSMs using HF orthogonal square-wave voltage injection into a stationary reference frame," *IEEE Trans. Power Electron.*, vol. 34, no. 3, pp. 2573–2584, Mar. 2019.

[17] Q. Tang, A. Shen, X. Luo, and J. Xu, "PMSM sensorless control by injecting HF pulsating carrier signal into ABC frame," *IEEE Trans. Power Electron.*, vol. 32, no. 5, pp. 3767–3776, May 2017.

[18] S.-I. Kim, J.-H. Im, E.-Y. Song, and R.-Y. Kim, "A new rotor position estimation method of IPMSM using all-pass filter on high-frequency rotating voltage signal injection," *IEEE Trans. Ind. Electron.*, vol. 63, no. 10, pp. 6499–6509, Oct. 2016.

[19] J. M. Liu and Z. Q. Zhu, "Novel sensorless control strategy with injection of high-frequency pulsating carrier signal into stationary reference frame," *IEEE Trans. Ind. Appl.*, vol. 50, no. 4, pp. 2574–2583, Jul./Aug. 2014.

[20] Z. Q. Zhu and L. M. Gong, "Investigation of effectiveness of sensorless operation in carrier-signal-injection-based sensorless-control methods," *IEEE Trans. Ind. Electron.*, vol. 58, no. 8, pp. 3431–3439, Aug. 2011.

[21] G.-D. Andreescu, C. I. Pitic, F. Blaabjerg, and I. Boldea, "Combined flux observer with signal injection enhancement for wide speed range sensorless direct torque control of IPMSM drives," *IEEE Trans. Energy Convers.*, vol. 23, no. 2, pp. 393–402, Jun. 2008.

[22] N. Bianchi and S. Bolognani, "Influence of rotor geometry of an IPM motor on sensorless control feasibility," *IEEE Trans. Ind. Appl.*, vol. 43, no. 1, pp. 87–96, Jan. 2007.

[23] X. Luo, Q. Tang, A. Shen, and Q. Zhang, "PMSM sensorless control by injecting HF pulsating carrier signal into estimated fixed-frequency rotating reference frame," *IEEE Trans. Ind. Electron.*, vol. 63, no. 4, pp. 2294–2303, Apr. 2016.

[24] B. Shuang, Z. Q. Zhu, and X. Wu, "Improved cross-coupling effect compensation method for sensorless control of IPMSM with high frequency voltage injection," *IEEE Trans. Energy Convers.*, vol. 37, no. 1, pp. 347–358, Mar. 2022.

[25] S. Kim, J.-I. Ha, and S.-K. Sul, "PWM switching frequency signal injection sensorless method in IPMSM," *IEEE Trans. Ind. Appl.*, vol. 48, no. 5, pp. 1576–1587, Sep./Oct. 2012.

[26] J. Lillo, F. Rojas, J. Pereda, and D. Verdugo, "Extended Kalman filtering for floating capacitor voltage estimation on triple star bridge cells," *IEEE Trans. Ind. Electron.*, vol. 72, no. 8, pp. 8646–8656, Aug. 2025.

Junli Huang (Graduate Student Member, IEEE) received the B.S. degree in electrical engineering in 2021 from Tsinghua University, Beijing, China, where he is working toward the Ph.D. degree in electrical engineering with the Department of Electrical Engineering.

His main research interests include signal injection sensorless control for interior permanent-magnet synchronous motor.

Shanming Wang (Senior Member, IEEE) received the B.S. and M.S. degrees in electrical engineering from Nanchang University, Nanchang, China, in 1993 and 1996, respectively, and the Ph.D. degree in electrical engineering from the Department of Electrical Engineering, Tsinghua University, Beijing, China, in 2001.

In 2001, he was with the Department of Electrical Engineering, Tsinghua University, where he is currently a Professor. His research interests include the analysis and control of electric machines, vibration analysis of electrical machines, hybrid excitation permanent-magnet machines, the simulation of ac machines and systems, and fault analysis for electric machines and their protection.

Wenmao Liu (Member, IEEE) was born in Shandong, China, in 1988. He received the Ph.D. degree in electrical engineering from the School of Electrical Engineering, Beijing Jiaotong University, Beijing, China, in 2022.

He is currently a Postdoctoral and an Assistant Research Fellow with the Department of Electrical Engineering, Tsinghua University, Beijing. His research interests include research on the synthesis of physical fields of large electrical machines and the model and parameters of synchronous generators.